

A MICROPOLAR METABEAM WITH NONLOCAL FEEDBACK CONTROL CIRCUITS

Qian Wu, Guoliang Huang

Department of Mechanical and Aerospace Engineering, University of Missouri, Columbia, Missouri
65211, USA

ABSTRACT

Active control schemes provide emergent wave properties and flexible tunability in mechanical systems. Here, we propose both analytically and numerically a non-Hermitian metamaterial system enabled by piezoelectric patches and electronic non-local feedback control. The metamaterial system is physically realized by a non-local micropolar beam with non-local feedback control. Since the non-local feedback control breaks spatial reciprocity, the proposed metabeam supports not only non-reciprocal flexural wave amplification and attenuation, but also non-Hermitian skin effect featuring bulk localized eigenmodes in the finite structure. The non-reciprocal amplification and attenuation phenomena are quantitatively predicted by band structure analyses under both the continuum and discrete spring-mass representation, which can be attributed to the work exchange between mechanical and electric works. The non-Hermitian skin effect and the associated bulk localized eigenmodes are characterized by a topological invariant. In addition, direction-dependent bending stiffness is also demonstrated in the non-local micropolar piezoelectric metabeam with proper transfer functions. The electronically controllable non-Hermitian metabeam could pave the ways for designing future systems such as synthetic biofilaments and membranes with feed-back control schemes.

Keywords: non-Hermitian metabeam, piezoelectric system, non-local feedback control scheme, non-reciprocal elastic wave propagation.

1. INTRODUCTION

Metamaterial refers to a type of artificial periodic structures, which comprises subwavelength unit cells serving as the building block [1]. In the past two decades, the study on metamaterial have been attracting tremendous attention from researchers in both academic and industrial communities, due to the extremely flexible parametric tunability. Metamaterials support emergent wave properties that do not exist in nature, such as negative refraction [1], non-reciprocal wave propagation [2], cloaking [3,4]. Potential applications, based on acoustic and elastic wave control and manipulation, include sound noise control [5], vibration mitigation [6], metasurfaces [7], and so forth. Different from the metamaterials which are based on local resonance, phononic crystals rely on Bragg scattering and operate at different scales comparable to operating wavelengths. Recent progress in the field of phononic crystals is primarily concentrated on phononic topological insulators which support topologically protected edge and corner modes [8-12]. It is believed that the potential applications of topological insulators may include acoustic and elastic energy harvesting [11] and lasing [13].

Thus far, most of the studies of metamaterials and phononic crystals are within the Hermitian limit. In a Hermitian system,

the impact of gain and loss is ignored. In the last two decades, non-Hermiticity has been gaining considerable attention in various physical areas, such as in photonics [14, 15], acoustics [16] and elastics [17, 18]. Classical wave systems with non-Hermiticity usually involve the interaction between gain and loss components. Under certain conditions, the non-Hermitian systems with well-organized gain and loss preserve parity-time (PT) symmetry and may exhibit purely real spectra, behaving exactly as Hermitian systems [19]. Considerable efforts have been put in the PT symmetric systems in which loss and gain are balanced. This kind of systems exhibit multiple singularities in the spectrum called exceptional points, at which several unconventional wave propagation phenomena take place, such as enhanced mechanical sensing [20], unidirectional invisibility [14, 17] and so on. Moreover, various physical realizations of the PT symmetric non-Hermitian systems have been reported in multiple areas, such as Fe-doped LiNbO₃ and InGaAsP [21], leaky waveguides and active microphone arrays [16], and piezoelectricity of LiNbO₃ [22]. Topological phase induced by non-Hermiticity has become very essential in recent years. The research on this area starts from the investigation of exceptional points on unique properties that do not exist in Hermitian topological phase [23, 24]. Further efforts have been put in delivering bulk-boundary correspondence principal for the emergent non-Hermitian topological phase [25]. Similarly to the Hermitian case, the newly developed non-Hermitian bulk-boundary correspondence principal predicts non-Hermitian skin effect, which manifests as localized edge states at the boundaries of a one-dimensional lattice. Unlike those of the Hermitian counterpart, the edge states of the non-Hermitian systems are distributed within the bulk bands. Direct experimental observations have been made in topoelectrical circuits [26] and quantum dynamics [27].

Recent work towards the elastic counterpart has been focused on the establishment of a one-dimensional non-Hermitian spring mass chain with non-local feedback interactions [28]. However, the direct physical realization still remains to be done yet. In this paper, we report a non-Hermitian metabeam system enabled by piezoelectric patches and electronic non-local feedback control schemes. The metabeam serves as the physical realization of a non-local micropolar elastic lattice characterized by non-local feedback control, which has not been reported yet. Since the non-local feedback control breaks spatial reciprocity, the proposed non-local micropolar metabeam supports non-reciprocal flexural wave amplification and attenuation, bulk localized edge modes and non-reciprocal flexural wave propagation induced by directional bending stiffness. The non-reciprocal amplification and attenuation result from the one-way energy exchange of mechanical and electric parts locked to certain propagation direction. The bulk localized edge modes are the consequence of the non-Hermitian skin effect and can be characterized by a well-defined winding number. The direction-dependent bending stiffness results from the unequal group velocities along opposite propagation directions, induced by the tilted real dispersion band. Both unconventional phenomena can be well characterized analytically under the long

wavelength assumption and demonstrated using numerical approach. We hope the tunable non-local micropolar piezoelectric metabeam with non-local feedback control, together with the continuum model, could pave the ways for designing future systems such as synthetic biofilaments and membranes with feed-back control schemes.

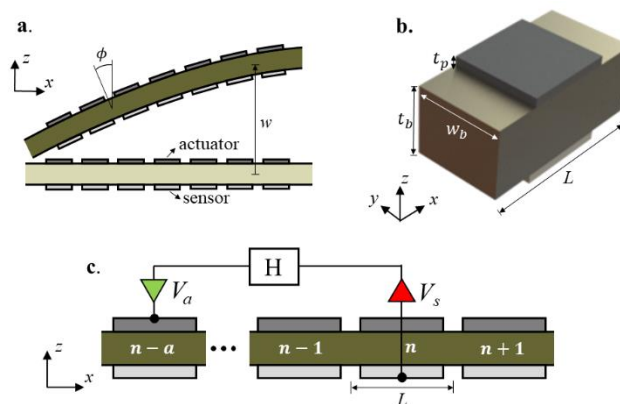


FIGURE 1: (a) Schematic illustration of one-dimensional non-Hermitian piezoelectric metabeam. The top and bottom piezoelectric patches serve as actuators and sensors, respectively. The motion of the metabeam can be described by two independent micropolar degrees of freedom: flexural displacement w and rotation angle ϕ . (b) Schematic of the metabeam unit cell with the white and gray piezoelectric patches attached on the host beam corresponding to the actuators and sensors, respectively. All the square patches are PZT-5J with a thickness $t_p = 0.55$ mm and a side length 4 mm. The beam is made of steel ($\rho_b = 7800$ kg/m³, $G_b = 79$ GPa, $E_b = 205$ GPa). Its geometrical property includes a unit cell size $L = 10$ mm, a thickness of $t_b = 3$ mm, and a width of $w_b = 4$ mm. The cross-sectional moment of inertia is $I_b = w_b t_b^3 / 12$. The two ends along the x direction are designated as Floquet periodic boundaries. (c) The n th sensor is connected to the $(n-a)$ th actuator through a transfer function H in a periodic way.

2. Design of the micropolar metabeam with non-local feedback control

We start with the design of the micropolar piezoelectric metabeam. The proposed structure consists of a thick host beam made of steel and multiple pairs of piezoelectric patches (PZT-5J) on top and bottom of the host beam [see Fig. 1(a)]. The corresponding unit cell serving as the building block is illustrated in Fig. 1(b). As we will deliver a continuum model for the metabeam, we mainly focus on low frequency region in which the long wavelength assumption well holds. The motion of the host beam can be characterized by two independent micropolar degrees of freedom, with one being the flexural displacement $w(x)$ of the midplane along the z axis and the other being the rotation angle $\phi(x)$ of the cross section with respect to the vertical axis [see Fig. 1(a)]. Each pair of PZT-5J patches serve as a sensor-actuator pair. As shown in Figs. 1(a) and 1(b), the PZT-5J patches, highlighted in white and gray, correspond to the sensors and actuators, respectively. The mechanical actuators apply elongation or contraction to the top surface of the host

beam, depending on the applied voltage. Instead, the sensor patches extract voltages from the elongation and contraction on the bottom surface of the host beam. The non-local feedback control is realized by connecting the n th sensor to the $(n-a)$ th actuator through a transfer function H , where a is integer and satisfies $a \geq 1$ [see Fig. 1(c)]. With this setup, the $(n-a)$ th actuator exerts an external bending moment which is proportional to the bending deformation within the n th unit cell, achieving non-locality and the following non-reciprocity .

3. Dispersion relation and non-reciprocity

Considering the lowest flexural band at low frequency, we can treat the discrete piezoelectric metabeam as a continuum model under the long wavelength assumption. Due to the shearing effect, the linearized continuum equations governing the flexural motion in the metabeam are given by

$$\rho \ddot{w} = \mu \partial_x^2 w - \mu \partial_x \phi \quad (1)$$

$$I \ddot{\phi} = \mu \partial_x w + B \partial_x^2 \phi + P \partial_x^2 \phi(x + \delta x, t + \delta t) - \mu \phi \quad (2)$$

where w and ϕ represent the z -directed flexural displacement and rotation angle. Other micropolar constants can be approximately determined as $\rho = \rho_b w_b t_b$, $\mu = \kappa G_b w_b t_b$, $B = E_b I_b$, $I = \rho_b I_b$, since the piezoelectric patches are much thinner than the host beam. Here, κ denotes the Timoshenko shear coefficient and equals 0.95 depending on the cross section of the host beam. Under the consideration of a Bloch wave solution $e^{i(kx - \omega t)}$ and assuming vanishing time delay $\delta t = 0$ for the feedback control, the above coupled partial differential equations can be rewritten into

$$\omega^4 - \left[\frac{\mu}{I} + \left(\frac{\mu}{\rho} + \frac{B+P'}{I} \right) k^2 \right] \omega^2 + \frac{(B+P')\mu}{I} k^4 = 0 \quad (3)$$

where $P' = P e^{ik\delta x}$ defines an additional bending stiffness for the piezoelectric metabeam and $\delta x = aL$. The value of $P = H\Psi$ can be determined numerically [29]. By applying prescribed rotation angles at finite frequencies to both ends of the unit cell in Fig. 1(b) and measuring the reaction moments on the ends, we can empirically find Ψ almost unchanged within the low-frequency range. For instance, $P = -0.23$ when $H = -15$. Solutions to Eq. (3) can be expressed as

$$\omega_{\pm}^2 = \frac{1}{2} \frac{\mu}{I} \left[1 + \left(\frac{I}{\rho} + \frac{B+P'}{\mu} \right) k^2 \pm \sqrt{\left(1 + \left(\frac{I}{\rho} + \frac{B+P'}{\mu} \right) k^2 \right)^2 - 4 \frac{(B+P')\mu}{I\rho} k^4} \right] \quad (4)$$

Equation (4) admits four solutions with two of them being the evanescent modes, and the other two as the propagating modes. Based on Eq. (4), we plot analytically the complex band structure for $a = 2$ and $P = -0.23$ in Fig. 3(a) and 3(b) (see the blue solid curves). The real part of the band structure is symmetric with respect to $k = 0$ and thus shows the reciprocal propagation along two opposite directions. However, its imaginary component is antisymmetric, meaning that the amplification and attenuation are non-reciprocal as the flexural modes propagate along the x axis. The flexural wave propagating in the $+x$ direction is first amplified at lower frequencies. As the frequency of the right-going mode exceeds the pseudo-Hermitian point around 17.8 kHz, the wave magnitude of the $+x$ propagation decays. In opposite, for the

left-going wave along the $-x$ direction, the magnitude first experiences amplification and then attenuation as the frequency increases. A consideration about work done by the non-local bending is useful in understanding the non-reciprocal process. Assume a harmonic solution $\phi(x) = \phi_0 \cos(\omega t - kx)$ for the micro-rotation degree of freedom. The non-local bending moment then reads $\Delta M = P \partial_x \phi(x + \delta x)$. In this case, the work done by the non-local bending moment within one period cycle can be determined by

$$W_E = \int \Delta M d\phi = -\pi k P \phi_0^2 \cos(k\delta x) \quad (5)$$

where we have assumed $x = 0$. Equation (5) suggests whether the non-local bending moment exerts positive or negative work depends on the sign of kP and the value of δx . When $\delta x \neq 0$, the non-locality exists and the non-reciprocal wave attenuation and amplification behaviors are related to the negative and positive work W_E done by the non-local bending moment, since W_E is an odd function of k . When $\delta x = 0$, the non-locality vanishes, and the non-zero W_E now corresponds to the hardening or softening of the metamaterial beam. In other words, the flexural amplification is a process in which electrical energy is converted into mechanical energy, while the flexural attenuation is a process where the mechanical energy is transferred into the electrical energy. To numerically validate the linearized continuum model, we also conduct eigenfrequency analysis using COMSOL Multiphysics for the unit cell shown in Fig. 1(b). In the simulation, Floquet boundary conditions are assigned on the two boundaries of the unit cell. The sensing signal collected from the bottom sensor after the transfer function H and later applied onto the actuator can be defined as $P \iint_{A_p} D_z dS / c_p e^{2ikl_b}$, where A_p , D_z and c_p represent the area of the piezoelectric shunts, z -directional electric displacement and intrinsic electric capacitance of the PZT-5J patches. One can see from Figs. 3(a) and 3(b) that the analytical and numerical results match very well, proving the correctness of our theoretical model. Note that the agreement at lower frequencies is better than that at higher frequencies, because of the long wavelength assumption we have made in the theoretical modeling.

It is intuitive to discretize the continuous micropolar piezoelectric metabeam into a discrete model. In this part, we consider the one-dimensional lattice whose unit cell consists of a rigid mass, a Hookean spring and a torsional spring; see Figs. 2(a) and 2(b). The vertical position and orientation of the n th rigid mass are represented by w_n and Φ_n , respectively; also see Fig. 2(b). The Hookean spring (red in Fig. 2(a)) connected to the n th mass causes a tension force reading

$$T_n = k_\mu (w_{n-1} - w_n + L\Phi_{n-1}) \quad (6)$$

While the torsional spring (blue in Fig. 2(a)) exert a bending moment of

$$\tau_n = k_B (\Phi_{n-1} - \Phi_n) \quad (7)$$

Since the micropolar metabeam is modulated by a nonlocal feedback control, an additional bending moment τ_n^a is added onto $(n-a)$ th unit cell, meaning that

$$\tau_n^a = p(\Phi_{n-1} - \Phi_n) \quad (8)$$

where $p = Pe^{ikL}/L$. In this design, the considered uniform distribution of bending moment does not necessarily cause shear force. Therefore, considering the equilibrium conditions within each unit cell, we can obtain

$$\begin{aligned} m\ddot{w}_n &= T_n - T_{n+1} \\ &= k_\mu(w_{n-1} - 2w_n + w_{n+1}) \\ &\quad + Lk_\mu(\Phi_{n-1} - \Phi_n) \end{aligned} \quad (9)$$

$$\begin{aligned} J\ddot{\Phi}_n &= \tau_n - \tau_{n+1} + \tau_n^a - \tau_{n+1}^a - LT_{n+1} = \\ &= (k_B + p)(\Phi_{n-1} - 2\Phi_n + \Phi_{n+1}) + Lk_\mu(w_{n+1} - w_n) - \\ &\quad L^2k_\mu\Phi_n \end{aligned} \quad (10)$$

The above two equations correspond to a finite-difference version of the governing equations given by Eqs. (1) and (2), with $m = \rho L$, $k_\mu = \mu/L$, $J = IL$, and $k_B = B/L$. To examine the discrete model, we can determine its dispersion relation in the complex frequency domain by assuming harmonic solutions for both w_n and Φ_n . The complex dispersion curves obtained, based on the discretized micropolar non-local metabeam model, are plotted in the insets of Figs. 3(a) and 3(b). excellent agreement between the numerical and discrete models only appears within lower frequency range, which can be well explained by the long-wavelength explanation.

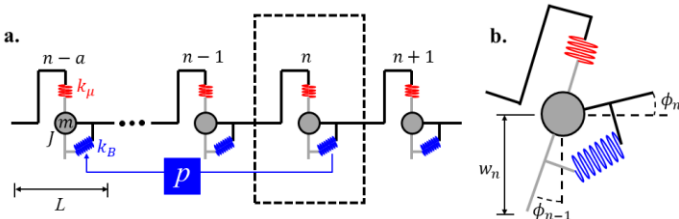


FIGURE 2: (a) Discrete spring-mass representation of the micropolar non-local piezoelectric metabeam. The discrete model consists of a central mass m with moment of inertial J , a Hookean spring k_μ (highlighted in red), a torsional spring k_B (highlighted in blue), and the lattice spacing L . (b) Schematic of the deformation of the n th lattice unit cell with w_n and Φ_n denoting as its flexural displacement and rotation angle, respectively.

In order to straightforwardly examine the effect of the transfer function H on the complex dispersion band, we introduce $l_1 = \sqrt{I/\rho}$, $l_2 = \sqrt{H/\mu}$ and $\omega_1 = \sqrt{\mu/I}$. Note that l_1 roughly corresponds to the thickness of the metabeam; l_2 defines the distance over which shearing and bending of equal transverse deflection cost equal amount of energy; finally, ω_1 sets a frequency scale separating transverse flexural modes and shear modes of higher frequencies. Replacing the notations and only considering the lowest flexural band yields

$$\omega_- = \frac{\omega_1}{\sqrt{2}} \sqrt{1 + a - \sqrt{(1 + a)^2 - b}} \quad (11)$$

in which $a = (l_1^2 + l_2^2 + P'/\mu)k^2$ and $b = 4l_1^2(l_2^2 + P'/\mu)k^4$. In our proposed metabeam, $l_1 \approx 10^{-4}$ m, and $l_2 \approx 10^{-3}$ m. For small wave number $k \ll [l_1(l_2 + P'/\mu)]^{-1/2}$, it

is easy to find that $b \ll (1 + a)^2$ and $a \ll 1$. Therefore, the above expression given by Eq. (11) can be approximated as

$$\omega_- = \Omega_1 P(\cos k\delta x + i \sin k\delta x) + \Omega_2 \quad (12)$$

where Ω_1 and Ω_2 take the forms

$$\Omega_1 = \frac{\omega_1}{B} \left[\frac{1}{2} l_2 \left(l_1 k^2 - \frac{1}{2} l_1^3 k^4 \right) - \frac{3}{4} l_1 l_2^3 k^4 \right]$$

$$\Omega_2 = \omega_1 \left[l_2 \left(l_1 k^2 - \frac{1}{2} l_1^3 k^4 \right) - \frac{1}{2} l_1 l_2^3 k^4 \right]$$

Ω_2 determines the dispersion of the unperturbed beam in the absence of feedback control ($H = 0$). When the non-local feedback is toggled on, a perturbation proportional to Ω_1 is applied. Close observation of Eq. (12) reveals that for a purely real P (or purely real H), $\text{Re}(\omega_-)$ is always symmetric. While $\text{Re}(\omega_-)$ is always antisymmetric, meaning that the attenuation and amplification are non-reciprocal. Also, multiple attenuation and amplification bands can be obtained if $a > 1$, owing to the odd sine function of $k\delta x$. In addition, one may select proper phase for H to make the real part of the band structure asymmetric. This corresponds to a directional bending stiffness, as we will discuss later.

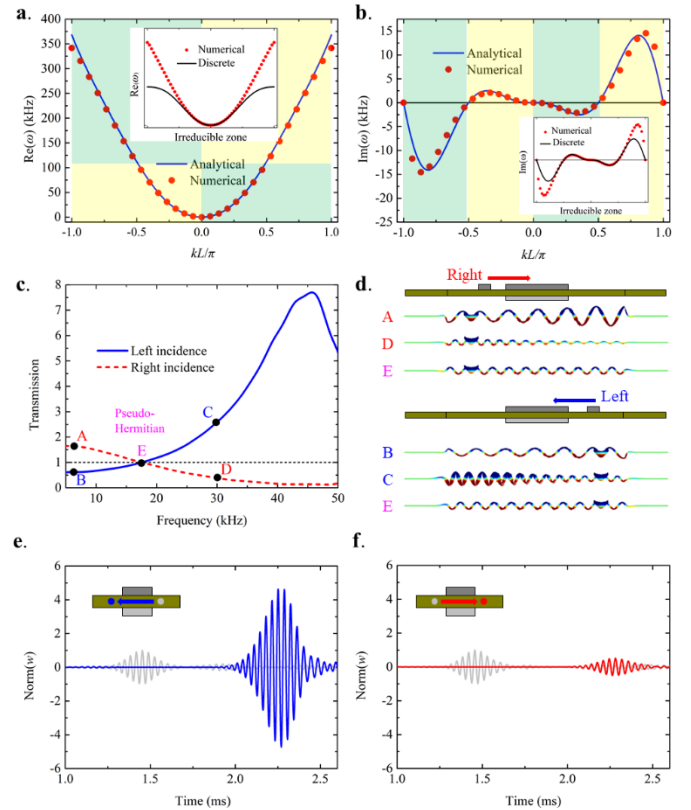


FIGURE 3: Complex dispersion relation of the nonlocal micropolar piezoelectric metabeam with nonlocal feedback control when $a = 2$. (a) Real part of the band structure. (b) Imaginary part of the band structure. In both figures, the green and yellow areas correspond to the attenuation and amplification regions, respectively. The insets illustrate the comparison between the theoretical discrete model and the exact numerical one. (c) Frequency dependent amplitudes of transmission for both propagation directions. Five representative cases are selected at 6,

17.8 and 30 kHz. (d) Flexural field distributions of the five selected points. The schematics illustrate the incident directions. (e) and (f) Transient analysis for both incident directions. Blue and red signals represent the transmission of the left and right incidence, respectively, while the gray ones indicate the 10-cycle tone burst incidences centered at 30 kHz.

To directly observe the non-reciprocity of our nonlocal micropolar metabeam, we construct a finite lattice with 12 unit cells. Two piezoelectric patches of the same geometrical and material properties as the sensors and actuators are employed to generate left- and right-going flexural modes [see the schematic illustrations in Fig. 3(d)]. The simulation model is terminated by perfect matched layers. We conduct frequency-domain analysis by sweeping the frequency from 5 to 50 kHz, in order to cover the range of interest. The transmitted flexural displacements w for the two propagation directions are recorded in function of frequency and later are normalized to the transmitted flexural displacement w_0 without any control ($H = 0$). Figure 3(c) clearly illustrates the left- and right-going flexural modes experience different changes in magnitude. For the lower frequency band ($f < 17.8$ kHz), the left-going mode experiences attenuation, while the right-going mode experiences amplification. Within the higher frequency region ($f > 17.8$ kHz), the scenarios for the left- and right-going modes switch. The frequency-domain results agree very well with the band structure analysis of the unit cell [see Fig. 3(a) and 3(b)].

We further extract the flexural field distributions at five representative points, as indicated in Fig. 3(c) and 3(d). The colormap scales of the flexural displacement in Fig. 3(d) are identical for a better comparison among these cases. For the left-going scenario, the flexural waves clearly experience attenuation at point B (6 kHz) and amplification at point C (30 kHz). At the same frequencies, the field distributions for the right-going waves (points A and D) exhibit the opposite outcome. Interestingly, even though the metabeam system involves non-Hermiticity due to the nonlocality, pseudo-Hermitian scenario takes place at certain frequencies. As indicated by Eq. (12), when $k\delta x = \pm\pi$ at $a = 2$ in this setup, the imaginary part of the corresponding frequency $\text{Im}(\omega)$ vanishes meaning the mechanical and electrical energy is balanced. In the current configuration, the Hermitian case occurs at 17.8 kHz, which well agrees with the prediction given by Fig. 3(a) and 3(b). Last, changing the sign of the purely real transfer function H will mirror the imaginary part of the band structure with respect to the irreducible zone center. This will in turn make the previously attenuated modes amplified, and vice versa.

Furthermore, transient analysis is later conducted for both propagation directions around 30 kHz. The incident signal is a 10-cycle tone burst centered at 30 kHz for both scenarios. The transfer function used reads

$$H(\omega) = \frac{H_0}{(i\omega/\omega_0)^2 + 2i\eta\omega/\omega_0 + 1} \quad (13)$$

where $H_0 = -15$, the cutoff frequency $\omega_0 = 60 \times 2\pi$ rad/s, and the damping coefficient $\eta = 0.6$. At the cutoff frequency, $\arg(P) = -\pi/2$. Below the cutoff frequency, the system with such a transfer function should behave quite similarly as the one

with the constant $H = -15$, as we have discussed. Indicated by the frequency-domain results shown in Fig. 3(c), the left- and right-going modes experience amplification and attenuation, respectively. From Fig. 3(e) and 3(f), one can immediately find that the corresponding transient analysis yields the same results: the waves from the right are amplified whereas the waves from the left are attenuated. This transfer function can be easily realized using electric circuit [29]. These results further prove the correctness of our theoretical and frequency-domain analysis and are instructive for the future experimental realization.

4. Non-Hermitian skin effect

Due to the antisymmetric $\text{Im}(\omega)$, the flexural modes propagate along the x axis with either attenuating or amplifying magnitudes, depending on the propagation direction. This can also manifest as the so-called non-Hermitian skin effect. For a complex frequency ω , the following topological index ν , called winding number of a dispersion band, can be defined:

$$\nu(\omega) = \frac{1}{2\pi i} \sum_{\alpha} \oint_{-\pi/L}^{\pi/L} \frac{d}{dk} \log[\omega_{\alpha}(k) - \omega] dk \quad (14)$$

where $\omega_{\alpha}(k)$ is the frequency of the α band. Here, the α band is selected as the lowest flexural band. From a geometrical standpoint, ν counts the number of times the dispersion loops of a dispersion band over the irreducible zone encircles the selected frequency. Its sign is dependent of the handedness of the loops: $\nu > 0$ if the rotation about the selected frequency is counterclockwise; $\nu < 0$ otherwise. The winding number is an indicator of whether there exists localized eigenmodes within the bulk bands in a finite one-dimensional lattice. A non-zero $|\nu|$ features the existence of localized eigenmodes, while $\text{sign}(\nu)$ determines which side the eigenmodes are localized on. First, we plot the dispersion loops of the lowest flexural band in Fig. 4(a) and 4(b) for $H = -15$ and $H = 15$, respectively. They represent the numerically obtained eigenfrequency evolution from the left boundary of the irreducible zone to the right in the complex domain [see Fig. 3(a) and 3(b)]. Comparison between the numerically obtained loops and those of the discrete model is illustrated in Figs. 4(c) and 4(d) to show the good agreement occurring at low frequencies. Taking Fig. 4(a) as an example, the two closed loops are formed with the smaller one travelling in a counterclockwise trajectory, while the larger one counterclockwise. Following Eq. (14), one can find the winding numbers for the two loops are $\nu = 1$ and $\nu = -1$, respectively. Any eigenmode encircled by the loop of $\nu = -1$ is localized on the left boundary of the finite lattice composed of this unit cell, whereas the loop of $\nu = 1$ leads to localized eigenmodes on the right boundary. For $H = 15$, we obtain similar results but with winding number of opposite sign attached to each loop; also see Fig. 4(b). The localizations of the eigenmodes are expected to be opposite to the case of $H = -15$.

To illustrate the localized eigenmodes, we construct numerically a finite metabeam including 30 sensor-actuator pairs. We conduct eigenfrequency analysis with fixed boundary condition applied on both ends. Representative frequencies are selected within the four loops [see points A, B, C and D in Fig. 4(e) and 4(f)]. The mode shapes at points A and B shown in Fig.

4(e) clearly suggest that a negative winding number yields a left-handed localized eigenmode, whereas a positive winding number corresponds to a left-handed localized eigenmode. As for points C and D in Fig. 4(f), the situations are similar but with the localizations being switched to the opposite sides, due to the winding numbers of opposite signs. It is important to mention that the localized eigenmodes in our non-Hermitian system are within the bulk bands, unlike the topological in-gap edge states in a Hermitian system. This property ensures that the bulk localized eigenmodes discussed here do not necessarily rely on specific boundary conditions of the finite lattice. That said, a fixed-free or free-fixed boundary condition still allows the occurrence of the bulk localized eigenmodes, more likely with some slight frequency shifts.

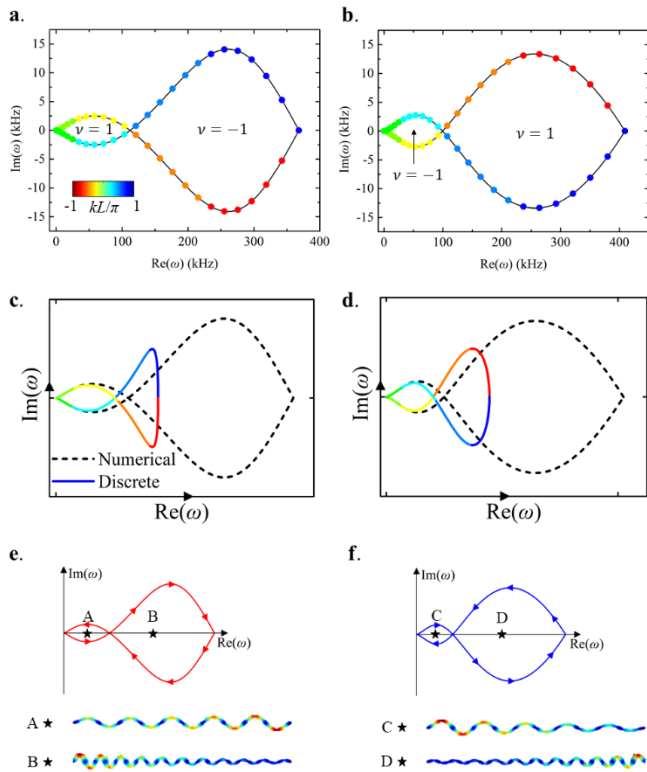


FIGURE 4: Non-Hermitian skin effect. The complex dispersion bands are displayed for (a) $H = -15$ and (b) $H = 15$. The winding number of each section v is indicated. (c) and (d) Comparison between the discrete and continuous numerical models. For both situations, two pairs of points, located closely and encircled by the two loops, are selected. The corresponding field distributions are illustrated in (e) and (f) for $H = -15$ and $H = 15$, respectively.

5. Directional bending stiffness

In the preceding section, the transfer function H was taken to be purely real. However, we can achieve a complex transfer function by introducing a phase delay. Let us assume $H = -15i$ for instance. Repeating the same analytical procedure of deriving the theoretical P , one can find roughly $P = -0.23i$. From Eq. (12), it can be readily seen that the real part of the perturbation from Ω_1 becomes an odd function. This outcome subsequently

“tilts” the real part of the unperturbed band structure that is described by Ω_2 , causing non-reciprocal flexural wave propagation with unequal group velocities. Following the previous analysis, we conduct both analytical modeling and numerical simulations for the unit cell shown in Fig. 1(b) when $H = -15i$. The results are present in Fig. 5(a). Great agreement can be found at low frequencies (see the blue solid and red dashed curves). Compared with the Hermitian scenario $H = 0$, the dispersion band for left- and right-going are shifted by different amounts of tilting. One can straightforwardly observe that the left-going flexural modes have larger group velocities than the right-going ones. This phenomenon can be directly related to the directional bending stiffness [29]. Also, the directional bending stiffness can be accessed in Eq. (3), where $B + P'$ contributes to the effective bending stiffness which indeed depends on the propagation direction.

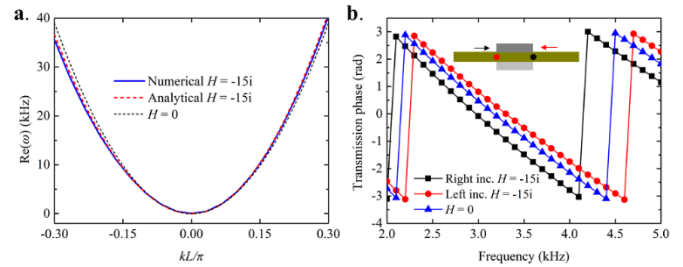


FIGURE 5: Directional bending stiffness. (a) Real part of the complex band structure for small wave numbers or for low frequencies. The red curved and black dotted curves correspond to the analytically obtained dispersion with $H = -15i$ and $H = 0$, respectively. The blue solid curve represents the numerically retrieved dispersion with $H = -15i$. (b) Output phase of the non-local micropolar metabeam containing 21 unit cells. The output phases for the left-going (red curve) and right-going (black curve) waves are collected at the right (black point) and left (red point) ends of the metabeam section, respectively.

Under the current parametric setup, the tilting of our metabeam cannot reach large values. To clearly demonstrate the directional bending stiffness and the associated non-reciprocal flexural wave propagation, we model a finite metabeam system similar to the one in Fig. 3(d), but with 21 sensor-actuator pairs included. We send in flexural excitations from both sides covering from 2 to 5 kHz, and numerically measure the output phase defined by $-i \log \left[\frac{i \text{Im}(w) + \text{Re}(w)}{|w|} \right]$ at the output plane, as shown in the inset of Fig. 5(b). The frequency-dependent output phases in Fig. 5(b) clearly demonstrate that for $H = -15i$, the phase differences from the Hermitian case of $H = 0$ are always positive for right-going flexural modes and negative for left-going ones. In other words, the wave number differs for the opposite directions, and so does the bending stiffness.

6. Conclusion

We investigate the implementation of the non-local metabeam system enabled by non-local feedback control circuits, providing a physical realization of the non-local micropolar elastic systems. Both the continuous and discrete models provide accurate description of the complex band

structure, when compared with numerical results. The non-reciprocal wave amplification and attenuation are numerically observed in both frequency- and time-domain analysis. It is revealed that the physical process of the attenuated and amplified propagation can be attributed to the energy exchange between the mechanical and electrical works. As a dynamic consequence, the non-Hermitian skin effect of the finite system is demonstrated and interpreted by the topology of the complex dispersion band. Last, by tuning the phase of the complex transfer function, non-reciprocal wave propagation characterized by directional effective bending stiffness can be realized. We believe this work can pave the ways for designing systems such as synthetic biofilaments and membranes with feed-back control schemes.

ACKNOWLEDGEMENTS

This work is supported by the Air Force Office of Scientific Research under Grant No. AF 9550-18-1-0342 and AF 9550-20-0279 with Program Manager Dr. Byung-Lip (Les) Lee and the Army Research Office under Grant No. W911NF-18-1-0031 with Program Manager Dr. Daniel P Cole.

REFERENCES

- [1] D. R. Smith, J. B. Pendry, M. C. K. Wiltshire, Metamaterials and negative refractive index, *Science*, 305 (2004) 788-793.
- [2] Q. Wu, H. Chen, H. Nassar, G. L. Huang, Non-reciprocal Rayleigh wave propagation in space-time modulated surface, *Journal of the Mechanics and Physics of Solids* 146 (2021) 104196.
- [3] X. C. Xu, Q. Wu, H. Chen, H. Nassar, Y. Y. Chen, A. Norris, M. R. Haberman, G. L. Huang, Physical observation of a robust acoustic pumping in waveguides with dynamic boundary, *Physical Review Letters* 125 (2020) 253901.
- [4] H. Nassar, Y. Y. Chen, G. L. Huang, A degenerate polar lattice for cloaking in full two-dimensional elastodynamics and statics, *Proc. R. Soc. A*, 474 (2018) 2219.
- [5] H. Nguyen, Q. Wu, X. C. Xu, H. Chen, S. Tracy, and G. L. Huang, Broadband acoustic silencer with ventilation based on slit-type Helmholtz resonators, *Applied Physics Letters* 117 (2020) 134103.
- [6] H. H. Huang, C. T. Sun, Wave attenuation mechanism in an acoustic meta material with negative effective mass density, *New Journal of Physics* 11 (2009) 013003.
- [7] Y. Y. Chen, X. P. Li, H. Nassar, G. L. Huang, A programmable metasurface for real time control of broadband elastic rays, *Smart Materials and Structures* 27 (2018) 115011.
- [8] S. Y. Yu, C. He, Z. Wang, F. K. Liu, X. C. Sun, Z. Li, H. Z. Lu, M. H. Lu, X. P. Liu, Y. F. Chen, Elastic pseudospin transport for integratable topological phononic circuits, *Nature Communications* 9 (2018) 3072.
- [9] S. H. Mousavi, A. B. Khanikaev, Z. Wang, Topologically protected elastic waves in phononic metamaterials, *Nature Communications* 6 (2015) 8682.
- [10] H. Chen, H. Nassar, G. L. Huang, A study of topological effects in 1D and 2D mechanical lattices, *Journal of the Mechanics and Physics of Solids*, (2018) 22-36.
- [11] Q. Wu, H. Chen, X. P. Li, G. L. Huang In-plane second-order topologically protected states in elastic kagome lattices, *Physical Review Applied* 14 (2020) 014084.
- [12] S. D. Huber, Topological mechanics, *Nature Physics* 12 (2016) 621.
- [13] G. Harari, M. A. Bandres, Y. Lumer, M. C. Rechtsman, Y. D. Chong, M. Khajavikhan, D. N. Christodoulides, M. Segev, Topological insulator laser: Theory, *Science* 359 (2018) 4003.
- [14] Z. Lin, H. Ramezani, T. Eichelkraut, T. Kottos, H. Cao, D. N. Christodoulides, Unidirectional invisibility induced by PT-symmetric periodic structures, *Physical Review Letters* 106 (2011) 213901.
- [15] L. Feng, Y.-L. Xu, W. S. Fegadolli, M. H. Lu, J. E. B. Oliveira, V. R. Almeida, Y. F. Chen, A. Scherer, Experimental demonstration of a unidirectional reflectionless parity-time metamaterial at optical frequencies, *Nature Materials* 12 (2013) 108–113.
- [16] C. Shi, M. Dubois, Y. Chen, L. Cheng, H. Ramezani, Y. Wang, and X. Zhang, Accessing the exceptional points of parity time symmetric acoustics, *Nature Communications* 7 (2016) 11110.
- [17] Q. Wu, Y. Y. Chen, and G. L. Huang Asymmetric scattering of flexural waves in a parity-time symmetric metamaterial beam, *The Journal of the Acoustical Society of America* 146 (2019) 850.
- [18] Z. Hou and B. Assouar, Tunable elastic parity-time symmetric structure based on the shunted piezoelectric materials, *Journal of Applied Physics* 123 (2018) 085101.
- [19] C. M. Bender and S. Boettcher, Real spectra in non-Hermitian Hamiltonians having PT symmetry, *Physical Review Letters* 80 (1998) 5243–5246.
- [20] M. I. N. Rosa, M. Mazzotti, M. Ruzzene, Exceptional points and enhanced sensitivity in PT-symmetric continuous elastic media, *Journal of the Mechanics and Physics of Solids* 149 (2021) 104325.
- [21] A. Guo, G. J. Salamo, D. Duchesne, R. Morandotti, M. Volatier-Ravat, V. Aimez, G. A. Siviloglou, D. N. Christodoulides, Observation of PTsymmetry breaking in complex optical potentials, *Physical Review Letters* 103 (2009) 093902.
- [22] L. Shao, W. Mao, S. Maity, N. Sinclair, Y. Hu, L. Yang, M. Lončar, Non-reciprocal transmission of microwave acoustic waves in nonlinear parity-time symmetric resonators, *Nature Electronics* 3 (2020) 267-272.
- [23] H. Zhou, C. Peng, Y. Yoon, C. W. Hsu, K. A. Nelson, L. Fu, J. D. Joannopoulos, M. Soljacic, B. Zhen, Observation of bulk fermi arc and polarization half charge from paired exceptional points, *Science* 359 (2018) 1009.
- [24] Y. Xu, S-T. Wang, L. M. Duan, Weyl exceptional rings in a three-dimensional dissipative cold atomic gas, *Physical Review Letters* 118 (2017) 045701.
- [25] T. E. Lee, Anomalous edge state in a non-Hermitian lattice, *Physical Review Letters* 116 (2016) 133903.

[26] T. Hofmann, T. Helbig, F. Schindler, N. Salgo, M. Brzezińska, M. Greiter, T. Kiessling, D. Wolf, A. Vollhardt, A. Kabaši, C. H. Lee, A. Bilušić, R. Thomale, T. Neupert, Reciprocal skin effect and its realization in a topoelectrical circuit, *Physical Review Research* 2 (2020) 023265.

[27] L. Xiao, T. Deng, K. Wang, G. Zhu, Z. Wang, W. Yi, P. Xue, Observation of non-Hermitian bulk-boundary correspondence in quantum dynamics, arXiv:1907.12566.

[28] M. I. N. Rosa, M. Ruzzene, Dynamics and topology of non-Hermitian elastic lattices with non-local feedback control interactions, *New Journal of Physics* 22 (2020) 053004.

[29] Y. Y. Chen, X. P. Li, C. Scheibner, V. Vitelli, G. L. Huang, Realization of active metamaterials with odd micropolar elasticity, arXiv: 2009.07329.